Investigation of MnO2 nanoparticles anchored 3D-Graphene Foam Composites (3DGF-MnO2) as an adsorbent for strontium adsorption using Central Composite Design (CCD) method

3 authors, including:

Sibel Kasap
Sabanci University
29 PUBLICATIONS   **108** CITATIONS

SEE PROFILE

Emine nostar aslan
Ege University
3 PUBLICATIONS   **11** CITATIONS

SEE PROFILE

Some of the authors of this publication are also working on these related projects:

Project   Investgation of adsorption capacity of 3D-graphene foam for radionuclides View project

NJC

Check for updates

Investigation of MnO₂ nanoparticles-anchored 3D-graphene foam composites (3DGF-MnO₂) as an adsorbent for strontium using the central composite design (CCD) method†

Sibel Kasap, [ID] *[a] Emine Nostar Aslan [ID] [b] and İbrahim Öztürk [ID] [b]

Strontium-90 is one of the dangerous fission products generated during electricity production in nuclear reactors and the separation of this radionuclide from contaminated water is an important step in safeguarding human health and minimizing the impact on the environment. In this research, the adsorption of strontium ions onto 3DGF-MnO₂ composites is investigated. Three-dimensional graphene foam (3DGF) was prepared by the chemical vapor deposition (CVD) method, then it was doped with MnO₂ nanoparticles by the hydrothermal method. The 3DGF-MnO₂ composite was characterized by Raman and XRD to reveal its chemical and structural properties. Raman and XRD results confirmed the functionalization of the three-dimensional graphene foam with β-MnO₂ nanoparticles. Furthermore, scanning electron microscopy showed that spindle-like agglomerated MnO₂ particles were decorated on the interconnected 3DGF surface. BJH analysis indicated that 3DGF possesses mesopores and the BET specific surface area of 3DGF was 34.01 m^2 g^{-1}. The effects of adsorption parameters on the adsorption process were evaluated by the response surface methodology (RSM) approach based on central composite design. The analysis of variance (ANOVA) results showed that the applied model was statistically significant due to high F (21.66) and very low P (<0.0001) values. Adsorption equilibrium isotherms were analyzed using the Langmuir, Freundlich and Dubinin–Radushkevich models. According to the Langmuir isotherm analysis, the maximum adsorption capacity of strontium ions on 3DGF-MnO₂ was estimated to be 47.39 mg g^{-1}. The mean adsorption free energy (E) was found to be 7.07 kJ mole^{-1} using the D–R model, indicating that the adsorption process occurs by physisorption. Finally, Thermo-dynamic parameters such as Gibbs free energy (ΔG°), the enthalpy (ΔH°) and the entropy change of adsorption (ΔS°) were also calculated and it was found that the adsorption process was spontaneous and exothermic in nature.

Introduction

During the operation of nuclear power facilities, large volumes of liquid waste, including radioactive isotopes such as cesium, strontium, iodine, cobalt, plutonium, are generated. Among them, ^{90}Sr is of particular concern due to its high cumulative fission yield (5–6%) and the emission of hazardous β-radiation. Strontium-90 has very strong water solubility and therefore, it can move with water down to the underlying layers of soil and into the groundwater. As a result, it affects the food chain from flora to fauna and humans. When it is taken into the human body through the food chain, it can easily replace calcium ions in the human bone tissue because of its chemical similarity to calcium and it continues to irradiate localized tissue causing many forms of cancer such as leukaemia and bone neoplasm. Hence, the removal of radioactive strontium from water is an important and challenging task for the nuclear power industry.[1–7]

The adsorption technique, including ion exchange, is considered one of the most versatile and effective approaches for the selective separation of radionuclides from high-level radio-active waste because of its high remediation yield, its practical and cheaper usage and good tolerability to radiation, chemical, thermal, and mechanical stress.[1,8–12] There are many kinds of materials (such as zeolites,[13,14] perlite and clay minerals,[15–19] nano-sized metal oxides including ferric oxides,[20] manganese oxides,[21,22] titanium oxides,[23–25] hydroxyapatite,[26] activated carbon[27,28] (AC), resin,[29] carbon nanotubes[30] (CNT), polymers[31] and graphene-based[32–34] materials) that have been shown in

^{a} *Sabanci University, Nanotechnology Research Center (SUNUM), Tuzla, İstanbul, Turkey. E-mail: skasap@sabanciuniv.edu*

^{b} *Ege University, Institute of Nuclear Sciences, Bornova, İzmir, Turkey*

† Electronic supplementary information (ESI) available. See DOI: 10.1039/c8nj05283b

literature to be selective radionuclide adsorbents. Among these adsorbents, nano-sized manganese oxides have demonstrated a large capacity for selectivity toward strontium ions in the presence of competitive ions, especially Na^+, K^+, Mg^{2+}, Ca^{2+}.[22,35] Therefore, nano-sized manganese oxides have drawn great attention as being among the most effective sorbents of strontium ions. However, like other nano-sized metal oxides, nano-sized manganese oxides are also prone to agglomeration due to van der Waals forces or other interactions. Therefore, they are not suitable in fixed beds or any other flow-through system. To improve the usability of these adsorbents, they need to impregnate porous supports.[36]

Nowadays, three-dimensional foam-like graphene-based structures have started to receive significant attention in adsorption technology because of their properties such as high surface area, low density, and porous structure with large pore volume.[37–40] The self-assembly method and chemical vapor deposition method are two main approaches to obtaining 3D graphene foam.[41,42] In the self-assembly method, natural graphite powder is initially converted into reduced graphene oxide (rGO) under strong chemical oxidants such as HNO_3, $KMnO_4$ and H_2SO_4. After that, rGO is used as a precursor to produce 3D graphene and graphene-based composites using different methods. Although rGO can be produced in large amounts and it has abundant surface functional groups, the hydrophobic rGO sheets are easily aggregated and restacked due to the partial removal of hydrophilic functional groups after the reduction of GO. In addition, the use of chemical oxidants brings some disadvantages such as toxicity, corrosiveness and the presence of non-carbon impurities in rGO. Due to these drawbacks, 3D graphene structures obtained from rGO yield limited performance.[43–45] In CVD, a carbonaceous source is decomposed into carbon atoms by hydrogen at high temperatures and the carbon atoms are deposited onto a porous metal substrate to form 3D graphene foams. With this method, more controlled, uniform, continuous and interconnected 3D network graphene structures can be obtained. Therefore, it is believed to be a specific candidate for adsorption technology. Although graphene foam obtained by the CVD method seems to bring many advantages to adsorption technology, the use of this material alone is limited to adsorption technology because of its lack of functional groups.[46–49] Therefore, it needs to be improved with other materials, such as metal oxides and polymers, for use in adsorption technology.

In conventional experimental methods, generally, the optimization of the operating parameters is carried out by only changing one parameter while keeping the others at a constant level. Hence, many experiments are required to find optimum levels for each parameter. As a consequence, these techniques have led to undesirable results such as time-consumption, expense, the consumption of reagents and materials etc. Moreover, interactions between the parameters are not revealed and thus, these techniques are insufficient for explaining the influences of parameters on the progress. Response Surface Methodology (RSM) is an experimental design technique based on a collection of statistical and mathematical methods. RSM can be useful when a combination of several independent variables and their interactions affect desired responses. In this technique, experiments are designed using an experimental design method such as Central Composite Design (CCD), Box–Behnken design, Plackett–Burman design to achieve adequate and reliable measurement of the response of a parameter, then the adequacy of the applied method is tested by analysis of variance (ANOVA).[50–52]

In this study, 3DGF-MnO_2 composites were developed as adsorbents and their capacity to adsorb strontium from aqueous media was investigated. Firstly, the 3DGF were obtained by the CVD method, and then they were decorated with MnO_2 nanoparticles via the hydrothermal method. In this way, adsorbents selective to strontium ions were obtained. The structural characterization of these materials was conducted by the Brunauer–Emmet–Teller technique (BET), Raman spectroscopy, X-Ray Diffraction (XRD), FT-IR spectroscopy and scanning electron microscopy (SEM), while magnetic properties were determined by vibrating sample magnetometer (VSM). The adsorption behaviour of the magnetic foams was investigated by two sets of experiments generated by the CCD method. Four independent parameters, namely, pH, initial Sr^{2+} concentration (C), shaking time and solid (3DGF-MnO_2) to liquid ratio (m/V) were chosen with the CCD method. To evaluate the effect of the parameters on the adsorption process, three-dimensional response surface plots were drawn. The significance of the CCD model and the effect of individual variables or the interactions of the variables were investigated by ANOVA. Optimum conditions were predicted by using a mathematical model. Experimental equilibrium data were fitted to the Langmuir and Freundlich isotherm models to describe the relationship between Sr^{2+} ions and the 3DGF-MnO_2 surface in solution. In order to explain the adsorption mechanism, the mean adsorption free energy (E) was calculated using the Dubinin–Radushkevich (D–R) isotherm model. Furthermore, thermodynamic parameters such as Gibbs free energy change (ΔG°), standard enthalpy change (ΔH°) and standard entropy change (ΔS°) were calculated at four different temperatures to evaluate the behaviour of the adsorption process versus temperature.

Experimental

Fabrication of 3D-graphene foams (3DGF)

Graphene foams were fabricated by the CVD method under vacuum. The fabrication procedures were carried out in a horizontal quartz tube with diameter of 120 mm and 1400 mm length. Nickel foams with 1.6 mm thickness ($\geq$95% porosity, 99.99% purity), purchased from Alantum Advanced Technology Materials, were used as templates. The foam pieces, cut into 10 mm × 10 mm dimensions, were placed horizontally in the central zone of the quartz tube. The quartz tube was initially evacuated using a dry pump to the base pressure of 2×10^{-2} Torr, followed by ramping the furnace temperature to 975 °C in 20 minutes under 100 sccm of H_2 and 275 sccm of Ar flow. After reaching the desired fabrication temperature, the foams were annealed for 10 min at constant temperature while

the gas flow was maintained to treat the nickel foam substrate for more uniform growth. Then, 50 sccm of CH_4 as a carbon precursor was delivered into the quartz tube for 12.5 min to grow graphene over the Ni foam surface. Finally, the samples were allowed to cool to ambient temperature under Ar gas flow.

To obtain free-standing graphene foam, the nickel template was etched in 1 M $FeCl_3$ solution for 24 hours. After complete etching of the nickel, graphene foams were transferred to deionized water/HCl mixed solutions where they were left for 24 hours to clean the $FeCl_3$ residues. Finally, the samples were taken out of the solution and dried at 80 °C for 30 min in an oven.

Preparation of 3DGF-MnO$_2$ composites

3DGF-MnO$_2$ composites were prepared by the hydrothermal method. Briefly, 0.05 moles of $KMnO_4$ and 0.02 moles of $MnSO_4 \cdot H_2O$ were dissolved in 50 mL H_2O_2 solution (1 : 1 molar ratio of H_2O_2 to distilled water) at room temperature. After the dark-brown solution was obtained, the graphene foam pieces were soaked in the solution, then the resulting mixture was transferred to a Teflon-lined stainless steel autoclave (100 mL) and the autoclave was maintained at 180 °C for 6 h. After the reaction was complete, the products were taken out from the vessel and washed with deionized water until pH = 7. Finally, the samples were dried at 80 °C for 12 hours.

Analysis

The crystalline structure and morphology of the samples were examined by Raman spectroscopy (Renishaw inVia Reflex), X-Ray Diffraction (Bruker AXS Advance), FT-IR (Perkin Elmer Spectrum) and SEM (Zeiss Gemini 1530) techniques. In order to identify the morphologies of graphene and MnO$_2$ nanoparticles, Raman data were collected using a 532 nm laser source with 2 μm spot size within the range of 100–3000 cm^{-1}. The XRD patterns were obtained at ambient temperature from the 2θ values measured within the range of 20°–80° under Cu Kα X-radiation (λ_{Cu} = 1.5406 Å). The SEM images were taken at 20 kV to observe the structure of the 3DGF-MNO$_2$ composites. The specific surface area of 3DGF-MNO$_2$ was determined by the Brunauer–Emmet–Teller (BET) surface area measurement technique (Micromeritics ASAP 2020) by using the nitrogen (N$_2$) adsorption–desorption multi-point method. The samples were degassed in the flowing N$_2$ atmosphere at 200 °C for 24 h before the measurements.

Design of experiments

To investigate the parameters for Sr adsorption onto 3DGF-MnO$_2$, a set of adsorption experiments was carried out according to CCD. pH (X_1), the initial concentration of Sr^{2+} (C) (mg mL^{-1}) (X_2), shaking time (min) (X_3) and ratio of solid (3DGF-MnO$_2$) to liquid (m/V) (mg mL^{-1}) (X_4) were chosen as 4 independent parameters, while the adsorption capacity of graphene foams was used as the response variable.

The selected parameters were applied at 3 levels (low, basal and medium) as −1, 0, +1 with six repeats at the central point and eight-star points of −2 and +2 for −α and +α, respectively.

The range and levels of independent parameters are summarized in Table S1 (ESI†). A total of 30 experiments in the CCD matrix were performed. Each experimental run was analysed and the responses were correlated by using the following equation, including linear and quadratic terms:[51,52]

$$y_i = a_0 + \sum a_i X_i + \sum a_{ii} X_{ii}^2 + \sum a_{ij} X_i X_j \qquad (1)$$

y_i represents the predicted response, a_0, a_i, a_{ii} and a_{ij} are the coefficients for constant offset, linear, quadratic, and inter-action effects, respectively, and X_i and X_j are the independent parameters.

ANOVA at the 95% confidence level was used to determine the effect of independent parameters on the response. The compatibility of the response surface model was improved by calculation of the determination coefficient (R^2). Significant differences were evaluated using Student's t-test and one way ANOVA at the probability level of 0.05. The 3-D surface plots were drawn to demonstrate the relationship and interaction between the independent parameters and the response. The optimal points were determined by solving the equation derived from the final quadratic model and grid search in RSM plots regarding the constraints in which the specific surface area was at its maximum level.[51,52]

Adsorption experiments

The effects of independent parameters on the adsorption process were investigated by batch experiments using 1000 mg L^{-1} of 88Sr (stable isotope) stock solution at a constant temperature of 25 °C. Experiments were conducted using a GFL 1086 water bath shaker equipped with a microprocessor thermostat. For each experiment, 0.001 g of adsorbent was added to the liquid phase. After reaching equilibrium, the adsorbents were separated from the liquid phase using blue ribbon filter paper. Final ion concentrations in liquid phases were determined by Perkin Elmer Optima 2000 DV model ICP-OES.

The adsorption capacity q_e (mg g^{-1}) was calculated using eqn (2):[53]

$$q_e \left(\text{mg g}^{-1} \right) = \frac{(C_0 - C_e) \times V}{m} \qquad (2)$$

where C_0 and C_e are the initial and equilibrium concentrations in solution (mg L^{-1}), respectively; V is the volume of solution (L) and m is the mass of adsorbent (g).

Results and discussion

Characterization of 3DGF and 3DGF-MnO$_2$ composites

The Raman spectra of 3DGF and 3DGF-MnO$_2$ composites are given in Fig. 1. Characteristic peaks of graphene, the 2D and G band, were observed at 2700 cm^{-1} and 1600 cm^{-1}, respectively.[54] After 3DGF-MnO$_2$ formation, one additional peak centred at 650 cm^{-1} appeared in the Raman spectrum, which corresponds to the β-phase of MnO$_2$,[55] verifying the incorporation of MnO$_2$ nanoparticles into the GF. The defect-related D band, which is associated with the quality of
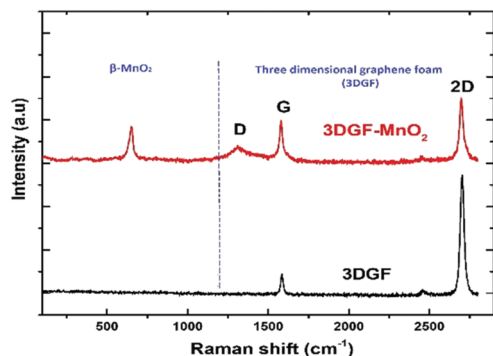
Fig. 1 Raman spectra of 3DGF and 3DGF–MnO$_2$ composites.

Fig. 3 SEM images of bare nickel (a), GF on nickel (b), 3DGF (c) and 3DGF–MnO$_2$ (d).

graphene, is suppressed in the 3DGF spectrum,[54] whereas, it is a prominent feature in the spectrum of 3DGF-MnO$_2$ (1325 cm^{-1}). This is because the attachment of MnO$_2$ NPs on the sp^2 hybridized planar carbon increases the disorder in the graphene crystal structure.

Fig. 2 shows the XRD spectrum of 3DGF and 3DGF-MnO$_2$ composites, respectively. All the intense peaks in the XRD pattern could be indexed using the JCPDS-ICDD. As shown in Fig. 2(a), two diffraction peaks at located 26.5° and 54.5°, namely (002) and (004) represent graphitic carbon. The diffraction peaks attributed to (110), (101), (200), (111), (210), (211), (220), (002), (310) and (112) represent the structure of β-MnO$_2$ (JCPDS card 81-2261). In addition, small diffraction peaks centred at 26.5° and 54.5°, corresponding to the graphitic phase,[56] can be seen in the spectrum.

The morphologies of 3D-GF and 3DGF-MnO$_2$ were examined by SEM, as shown in Fig. 3. In Fig. 3b, the graphene domains are clearly seen on the nickel foam surface, where dark and pale domains represent multilayer and single layer graphene respectively. Fig. 3c displays the SEM image of graphene foam without the nickel template. As revealed by the SEM image, graphene foam retains the structure of the nickel template with interconnected 3D characteristics and its skeleton shows a continuous structure. Fig. 3d shows that the skeleton of 3DGF is covered by spindle-like MnO$_2$ clusters.

The Brunauer–Emmett–Teller (BET) specific surface area and pore size measurements of 3DGF-MnO$_2$ were studied by
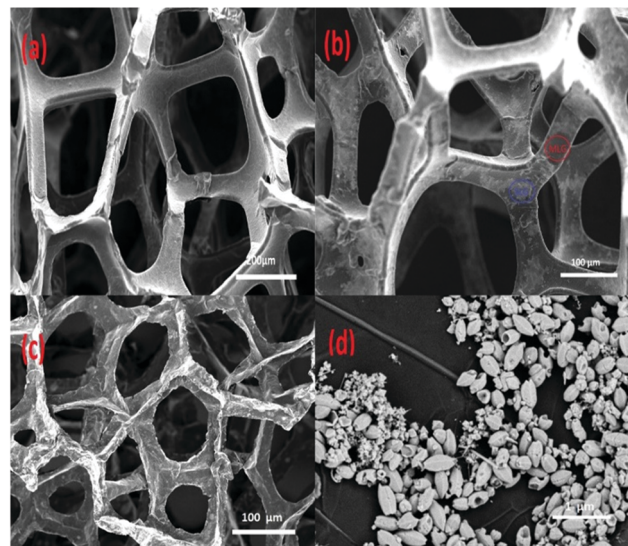
N$_2$ absorption/desorption. Fig. S1 (ESI†) shows the N$_2$ adsorption/desorption isotherm and the corresponding BJH pore-size distribution curve of the 3DGF-MnO$_2$. According to the isotherm, the BET specific surface area of the composite was calculated as 34.01 m^2 g^{-1}, which was smaller than that of the 3D-GF (295.55 m^2 g^{-1}) (Fig. S2, ESI†). The cumulative pore volume and the average pore size were calculated as 0.0994 cm^3 g^{-1} and 8.07 nm, respectively, using the Barrett Joyner Halenda (BJH) analysis. Furthermore, the isotherm was classified as type IV, according to IUPAC classification, indicating the presence of mesopores.[57]

The weight percentage of each component in the 3DGF-MnO$_2$ was calculated using TGA graphs (Fig. 4). The TGA curve of pure 3D-graphene foam showed about 76.3% weight loss at around 580 °C. On the other hand, 23.7% weight remained due to the residual nickel. Based on the TGA curve of MnO$_2$, the total weight loss was calculated to be 18.84% and two-step weight loss appeared in the curve. The first step indicates an 11.1% weight loss upon heating from room temperature to
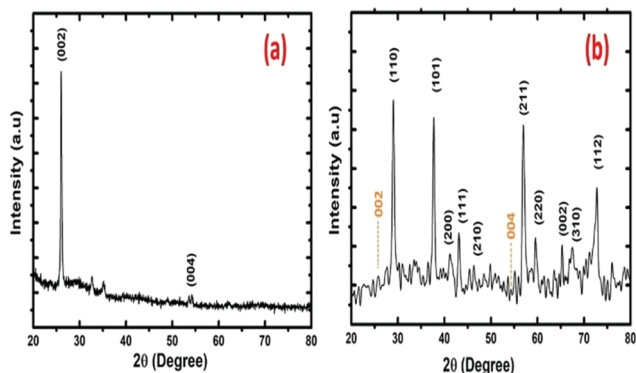

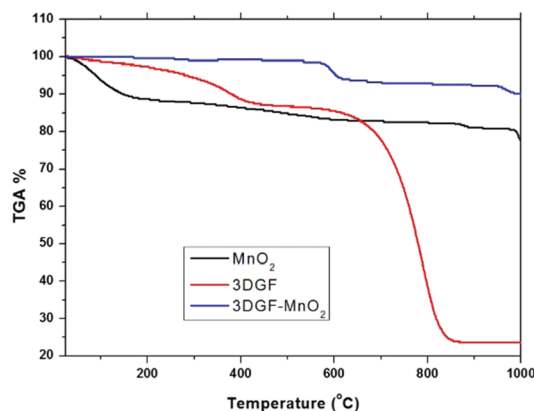Fig. 2 XRD spectra of 3DGF (a) and 3DGF–MnO$_2$ composites (b).

Fig. 4 TGA curves of 3DGF, MnO$_2$ and 3DGF–MnO$_2$.

195 °C, attributed to the removal of adsorbed water. Subsequently, weight loss of about 2% occurred in the temperature range of 518 °C to 910 °C, which indicated the transformation of MnO_2 into Mn_2O_3 with 2.5% weight loss. Due to the catalytic effect of manganese oxides, the combustion temperature of carbon for 3DGFMnO$_2$ started at 545 °C, which is lower than 3D-GF. The mass ratio of MnO_2 to graphene in the composite MG-3000 was calculated to be 8 : 1.

Statistical analysis and fitting model

The CCD matrix of four independent factors along with experimental and predicted responses is shown in Table S2 (ESI†). The second-order polynomial equation was drawn between the response variable and the input factors to explore the mathematical relationship between independent factors and response variable (capacity (mg g^{-1})):

$$y = 7.84 + 2.47X_1 + 0.24X_2 + 0.06X_3 - 19.88X_4 + 0.11X_1^2$$
$$- 6.52 \times 10^{-4}X_2^2 - 2.28 \times 10^{-4}X_3^2 + 8.38X_4^2 + 4.41$$
$$\times 10^{-3} \times X_1X_2 - 0.02X_1X_3 - 1.14X_1X_4 + 3.98$$
$$\times 10^{-4}X_2X_3 - 0.06X_2X_4 + 0.05X_3X_4 \tag{3}$$

The ANOVA (analysis of variance) study demonstrates that the regression model is highly significant as a large F value and a very low P value.[50,52,58] Therefore, the statistical importance of the applied model was investigated using the F-test for ANOVA with a 95% confidence level ($P < 0.05$) in this study. Table S3 (ESI†) indicates the ANOVA analysis for the applied model. For this process, the p-value was found to be less than 0.0001 and the F value was 21.66 for the model. These results indicate that the applied model is statistically significant. The R^2 value of 0.91 indicates that the applied model is at the 95% confidence level.

The p-values and regression coefficient were analysed by Student's t-test and one way ANOVA at the probability level of 0.05 to explain the significance of the effects of the parameters and their interactions on the response variables.[50,52,58] As can be seen in Table S4 (ESI†), the linear terms of three parameters (X_1, X_2, X_4) are given; the interaction effects between X_1X_3 and the quadratic effects of X_2 and X_4 were found to be statistically significant ($p < 0.05$) in the adsorption process.

The relationship between the experimental and the predicted values of response is presented in Fig. 5. The correlation value for the graph was calculated as $R^2 = 0.95$. This high correlation ($R^2 = 0.95$) value depicts high coordination between the experimental and predicted results within the range of the experiment.

The sign of the regression coefficient is an important parameter for finding the effects of independent values on responses.[50,52,58] It can be seen from Table S4 (ESI†) that the coefficient values for linear terms of two parameters including X_1 (pH) and X_2 (initial concentration of Sr^{2+}) and the quadratic effect of X_4 have a positive sign. Based on these results, it can be said that these three terms showed significant positive effects on adsorption process, meaning that the adsorption capacity increases with increases in these terms. On the other hand, the parameter X_4 (ratio of solid (3DGF-MnO$_2$)/liquid)
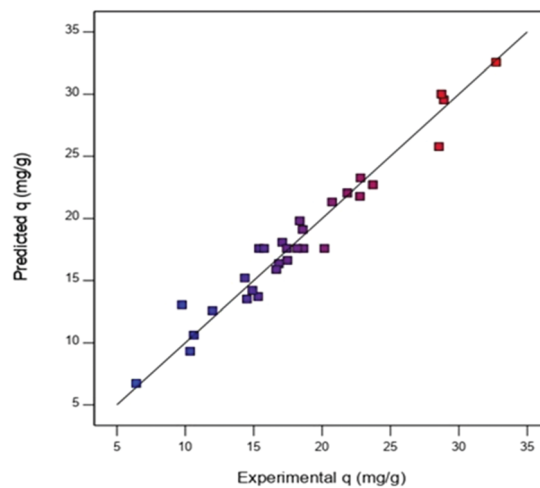

Fig. 5 The graph of experimental results *versus* predicted results.

showed a negative effect on the adsorption process, *i.e.*, the adsorption capacity was decreased with increasing these terms.

The 3D-response surface plot (3D-RSP) is a graphical representation of the regression equation; it shows combinations of two tested variables when the others are kept at their zero levels. This plot is useful for investigating desirable response values and operating conditions. In this way, the interaction between each independent variable can be understood easily and the optimal values of parameters can be determined.

The 3D-response surface plots of interactions between independent parameters on adsorption capacity (mg g^{-1}) were plotted in Fig. 6(a)–(f).

The effect of pH. Adsorption principally occurs by the electrostatic attraction between a solid surface and ions and it is well known that pH is a key effective factor in the process. As the pH of the solution changes, the surfaces of the 3DGF-MnO$_2$ composites undergo protonation or deprotonation:[59]

$$\equiv MnOH_2^+ \rightleftarrows \; \equiv MnOH + H^+ \tag{4}$$

$$\equiv MnOH \rightleftarrows \; \equiv MnO^- + H^+ \tag{5}$$

At lower pH values, protonation is the dominant mechanism. Positively charged sites on 3DGF-MnO$_2$ in this study enhance the repulsion forces between the sorbent surface and the Sr^{2+} ions and results in the reduction of the adsorption capacity. On the other hand, the sorbent surface undergoes deprotonation at higher pH values. Due to increased negatively charged sites on the sorbent, attractive forces between the surface and Sr^{2+} ions increase, causing an increase in the adsorption capacity. The effects of pH and initial Sr^{2+} concentration (C), shaking time and ratio of solid (3DGF-MnO$_2$)/liquid (m/V) on Sr^{2+} adsorption are shown in Fig. 6a, b, and c, respectively. As can be seen from these figures, the adsorption capacity rises with increasing pH.

The effect of the initial concentration of Sr^{2+}. The interactions of the initial concentration with other parameters are represented in Fig. 6a, d and e, respectively. As can be seen in these figures, the adsorption capacity is increased with
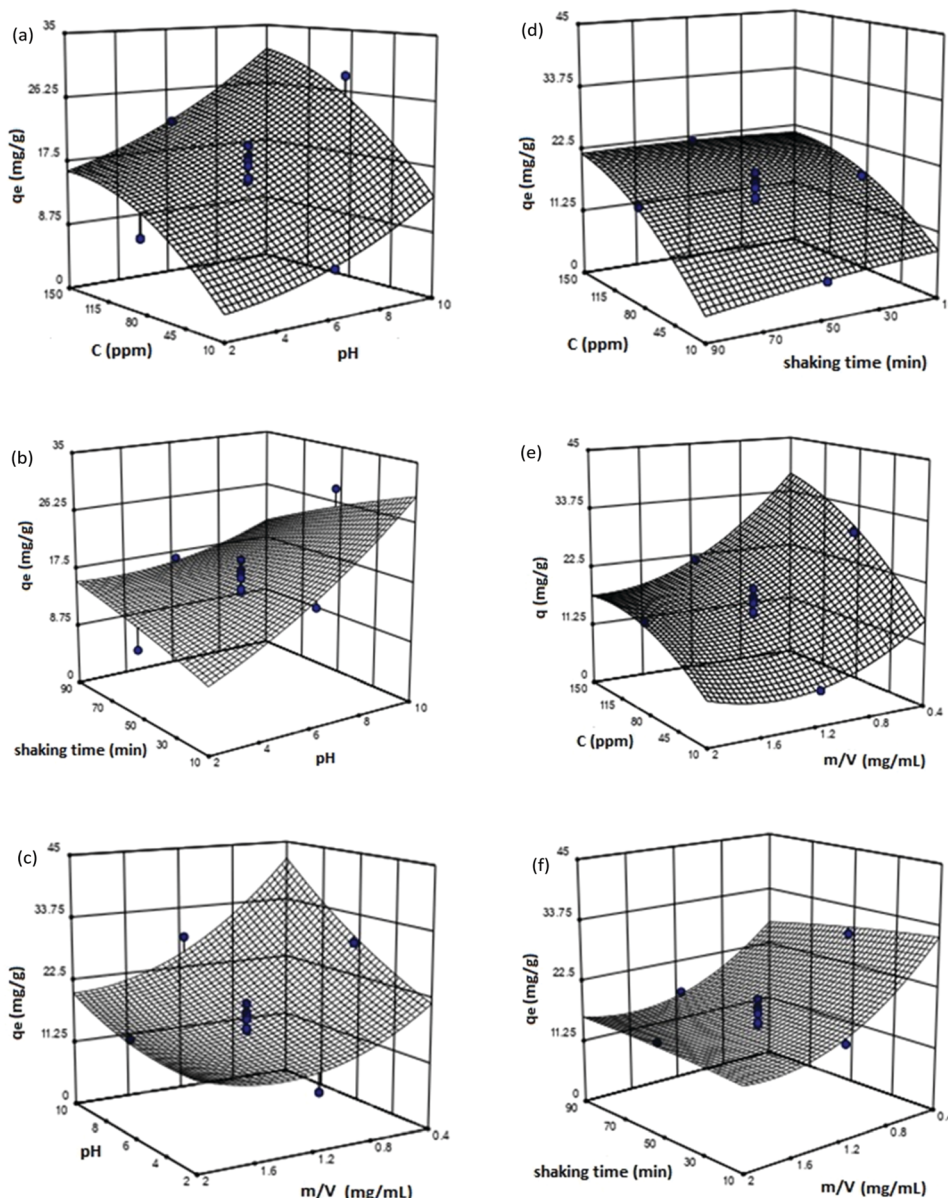
Fig. 6 (a) Effect of the interaction between pH and initial Sr^{2+} concentration (C (ppm)). (b) Effect of the interaction between pH and shaking time (min). (c) Effect of the interaction between pH and ratio of solid/liquid (m/V (mg mL^{-1})). (d) Effect of the interaction between initial Sr^{2+} concentration (C (ppm)) and shaking time (min). (e) Effect of the interaction between initial Sr^{2+} concentration (C (ppm)) and solid/liquid (m/V (mg mL^{-1})). (f) Effect of the interaction between solid/liquid (m/V (mg mL^{-1})) and shaking time (min).

increasing the initial concentration, then it starts to decrease slightly when the initial concentration is increased. At the beginning of the adsorption process, more favourable sites on the sorbent are available and therefore, more Sr^{2+} ions are imprisoned on the sorbent surface. However, the available sites on the sorbent surface become fewer with increasing ion concentration, and hence, the adsorption capacity of Sr^{2+} ions is decreased. In this study, the maximum adsorption capacity for each experiment was reached at 80 ppm of initial Sr^{2+} concentration.

The effect of shaking time. To investigate the effect of shaking time on the adsorption process in this study, experiments were conducted between 10 to 90 min. The interactions of shaking time with other parameters are given in Fig. 6b, d and f, respectively. As can be seen in these figures, the adsorption capacity shows a slight increase and then a slight decrease between 10 to 70 min. We concluded that the effect of shaking time on the adsorption process is unimportant.

The effect of the solid (3DGF-MnO$_2$)/liquid ratio (m/V). In order to examine the effect of m/V on the adsorption process, a couple of batch experiments were carried out for m/V in the range of 0.2–2 mg g^{-1}. In the experiments, the volume of Sr^{2+} solution was changed in the range of 0.5–2.5 mL, while the adsorbent dosage was kept constant at 10 mg. Fig. 6c, e and f present the interactions of the m/V with other parameters in the adsorption process. As depicted in the figures, the adsorption

capacity decreased as the m/V increased. This is because the active sites on the adsorbent decreased as the liquid volume increased, thus the adsorbent (3DGF-MnO$_2$) reached saturation.

Determination of the optimum adsorption parameters

To determine the maximum adsorption capacity of Sr^{2+} ions on 3DGF-MnO$_2$, the optimum values of the adsorption parameters were evaluated by eqn (3). In Table S5 (ESI†), optimum values of parameters are given. Based on these conditions, the maximum adsorption capacity was calculated as 63.44 mg g^{-1}.

Adsorption isotherms

Adsorption isotherms are a useful method for understanding adsorption mechanisms, surface properties, and the affinity of the adsorbent towards the adsorbate. They can also be used to evaluate the adsorption capacities of the different sorbents for pollutants in aqueous media.[53,57] In this study, three well-known adsorption isotherms, namely, Langmuir, Freundlich and Dubinin–Radushkevich (D–R), were used in order to investigate the adsorption mechanism.

The Langmuir isotherm model is the most commonly used model. According to this model, active sites on the adsorbent surface are limited and they are homogeneously distributed on the surface; therefore, adsorption can only occur at definite sites as a monolayer and there is no interaction between adsorbed molecules. On the other hand, the Freundlich isotherm model assumes that adsorbed molecules interact with each other, thus multilayer formation occurs on the solid surface. The linearized Langmuir and Freundlich equations are given in eqn (6) and (7), respectively.[53,57]

$$\frac{C_e}{q_e} = \frac{1}{q_{max}K_L} + \frac{1}{q_{max}}C_e \qquad (6)$$

q_e (mg g^{-1}) is the adsorbed Sr^{2+} amount at equilibrium, C_e (mg L^{-1}) is the supernatant concentration at the equilibrium, and q_{max} (mg g^{-1}) and K_L (L mg^{-1}) are constants representing the maximum adsorption capacity and the Langmuir constant related to the heat of adsorption, respectively.

$$\ln q_e = \ln K_f + \frac{1}{n} \ln C_e \qquad (7)$$

K_f (L g^{-1}) is a constant related to the adsorption capacity and $1/n$ is an empirical parameter related to the adsorption intensity.

Fig. 7 shows the Sr^{2+} adsorption isotherms of 3D-MGF; there was a good fit with both isotherm models. However, based on the value of the correlation coefficient, R, the adsorption mechanism of Sr^{2+} on 3D-MGF can be explained by the Freundlich model. The Freundlich isotherm model assumes a heterogeneous adsorption reaction. Hence, the Sr^{2+} adsorption capacity of 3D-MGF does not depend on the number of binding sites. Also, the adsorbed Sr^{2+} molecules interacted with each other and a multilayer formation occurred on the 3D-MGF surface. In addition to this, the adsorption affinity can be predicted by a dimensionless empirical parameter n. Adsorption occurs favourably when $1/n$ is between 0.1–1, whereas adsorption is
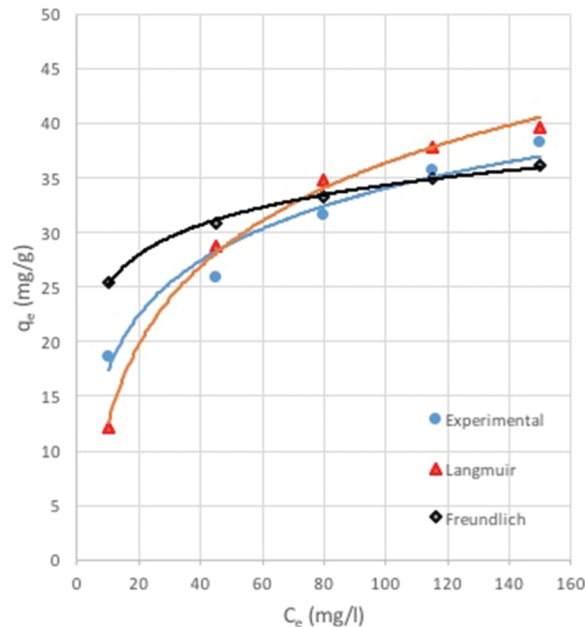

Fig. 7 Adsorption equilibrium data fitted with the Langmuir and Freundlich adsorption isotherm models (C_e: concentration of Sr^{2+} ions at equilibrium, q_e: adsorption capacity at equilibrium).

more difficult when $1/n$ is greater than 2. In this experiment, $1/n$ was calculated as 0.13. This means that the examined sorbent was favoured the uptake of Sr^{2+}, with calculated maximum adsorption capacity of 47.39 mg g^{-1}.

The D–R isotherm model is used to determine whether the adsorption is physical or chemical. The linearized D–R isotherm equation is represented as eqn (8):[53]

$$\ln q_e = \ln q_m - \beta\varepsilon^2 \qquad (8)$$

where q_e (mg g^{-1}) is the number of metal ions adsorbed at equilibrium, q_m (mg g^{-1}) is the maximum adsorption capacity, β is the activity coefficient related to the mean adsorption energy (mg^2 J^{-2}), and ε is the Polanyi potential. The constant b gives an idea about the mean adsorption free energy E (kJ mole^{-1}), which can be calculated using the relationship and the E (kJ mole^{-1}) value gives information about the adsorption mechanism, physical or chemical. If E is in the range of 8–16 kJ mole^{-1}, chemical forces are driving the adsorption process and the process is called chemisorption. In the case where E is lower than 8.0 kJ mole^{-1}, physical forces affect the sorption mechanism and the process is called physisorption.[57]

$$E = \frac{1}{\sqrt{-2\beta}} \qquad (9)$$

The D–R parameters are represented in Table S7 (ESI†), where it can be seen that the value of E for Sr^{2+} ions was calculated as 7.07 kJ mole^{-1}, which indicates that the adsorption mechanism was carried out by physical forces and therefore, the adsorption of Sr^{2+} onto 3DGF-MnO$_2$ is physisorption.

Thermodynamic studies

Thermodynamics studies are a good way to obtain information about the effects of temperature on the adsorption process. In order to determine this effect on the adsorption process, thermodynamic parameters such as Gibbs free energy change ($\Delta G°$), standard enthalpy change ($\Delta H°$) and standard entropy change ($\Delta S°$) are used. The Gibbs free energy change ($\Delta G°$) is given by the following equation:[53,57]

$$\Delta G° = -RT \ln K_d \qquad (10)$$

where K_d is the sorption equilibrium constant, R is the ideal gas constant (kJ mole^{-1} K^{-1}) and T is the absolute temperature (K).

The values of enthalpy change ($\Delta H°$) and entropy change ($\Delta S°$) are calculated from the slope and intercept of the plot of $\ln(K_d)$ *versus* $(1/T)$ using eqn (11):

$$\ln K_d = \frac{\Delta S}{R} - \frac{\Delta H}{RT} \qquad (11)$$

In this study, the effects of temperature on Sr^{2+} adsorption onto 3DGF-MnO_2 were investigated at temperatures ranging from 293 K to 333 K. The thermodynamic parameters of the adsorption process are listed in Table S8 (ESI†).

The negative values of $\Delta H°$ and $\Delta G°$ indicate that the Sr^{2+} adsorption process on 3DGF-MnO_2 is exothermic and spontaneous in nature.[53,57] It can be seen from Table S8 (ESI†) that the value of $\Delta G°$ decreased with increasing temperature. This behaviour could be due to the adsorption process requiring less energy at higher temperatures. The entropy change ($\Delta S°$) for the system was calculated as 0.02 J mole^{-1} K^{-1}. Although this value is positive, it is very small. This very small $\Delta S°$ value shows that the irregularity at the solid–liquid interface is minimum during the adsorption process. Additionally, the positive sign of $\Delta S°$ indicates that the metal ions displace more mobile ions from the adsorbent surface during the adsorption process.[53,57]

Conclusion

A three-dimensional graphene framework was prepared in the form of a foam for application in strontium adsorption from aqueous solutions. The foam-like 3DGF structures were fabricated using nickel foam as a template by a template-directed CVD method. The MnO_2 nanoparticles were incorporated into the 3D networks by the hydrothermal method to provide strontium with selectivity for the foam.

In order to optimize the parameters for Sr^{2+} adsorption onto 3DGF-MnO_2 composites, the CCD method was used. Under the optimized adsorption parameters, the adsorption capacity was found to be 47.39 mg g^{-1}. The Freundlich isotherm model best fit the adsorption process. The thermodynamic parameters showed that the adsorption process was spontaneous ($\Delta G° < 0$) and exothermic ($\Delta H° < 0$) in nature. In addition, the irregularity at the solid–liquid interface was minimal during the adsorption process.

Consequently, our findings show that 3DGF-MnO_2 composites have good potential for the removal of radionuclide pollutants *via* adsorption processes. In particular, due to their continuous micro-, meso-, and macrostructures, we believe that 3DGF-MnO_2 will be a new generation of materials in column separation. In addition, with the improved mechanical strength, it can also be used as a barrier material for geotechnical application in nuclear waste management.

Conflicts of interest

There are no conflicts to declare.

Acknowledgements

Notes and references

1 IAEA, IAEA safety standards series, SSR-5, 2011, 454–458.
2 R. Jankowiak, G. J. Small, V. N. Fleurov, A. P. Young, D. Stein, K. H. Fischer, J. A. Hertz, W. Atkins, R. Elber, M. Karplus, N. Go, J. Jackle, M. F. Shlesinger, J. T. Bendler, L. D. Grandine, E. R. Fitzgerald, D. Joseph, M. Karplus, R. Fiber, M. Karplus, D. A. Case, R. Elber, M. Karplus, J. J. Hopfield, V. Srajer, P. M. Champion, D. Rousseau, P. V. Argade, D. L. Rousseau, J. M. Friedman, T. G. Spiro, P. J. Steinbach, R. D. Young, J. D. Simon, J. M. Friedman, O. Binding, C. Ho, P. G. Wolynes, P. G. Wolynes, M. Gutin, P. G. Wolynes, A. M. Gutin, I. Kanter, P. G. Wolynes, H. Orland, F. Lainee, M. Mezard, M. Virasoro, G. J. Koper, H. Hilhorst, C. Levinthal, D. Thirumalai, P. G. Wolynes, J. H. Gibbs and J. Knowles, *Science*, 1991, **618**, 1603–1607.
3 D. Venables, N. F. Pidgeon, K. A. Parkhill, K. L. Henwood and P. Simmons, *J. Environ. Psychol.*, 2012, **32**, 371–383.
4 T. N. Srinivasan and T. S. G. Rethinaraj, *Energy Policy*, 2013, **52**, 726–736.
5 M. Aoki and G. Rothwell, *Energy Policy*, 2013, **53**, 240–247.
6 J. I. M. De Groot, L. Steg and W. Poortinga, *Risk Anal.*, 2013, **33**, 307–317.
7 P. C. Burns, R. C. Ewing and A. Navrotsky, *Science*, 2012, **335**, 1184–1188.
8 R. O. Abdel Rahman, H. A. Ibrahium and Y. T. Hung, *Water*, 2011, **3**, 551–565.
9 International Atomic Energy Agency, IAEA Technical reports series No. 408, 2002, 115.

10 I. Atomic and E. Agency, *IAEA-TECDOC*, 1992, vol. 675, pp. 1–189.

11 B. Robinson, *Water Supply Paper*, 1962, p. 131.

12 T. a Todd, T. a Batcheller, J. D. Law and R. S. Herbst, *Chemical Processing*, 2004.

13 H. Yeritsyan, A. Sahakyan, V. Harutyunyan, S. Nikoghosyan, E. Hakhverdyan, N. Grigoryan, A. Hovhannisyan, V. Atoyan, Y. Keheyan and C. Rhodes, *Sci. Rep.*, 2013, **3**, 1–7.

14 D. Bish, *Natural Microporous Materials in Environmental Technology*, 1999, vol. 362, pp. 177–191.

15 R. Akkaya, *Desalination*, 2013, **321**, 3–8.

16 M. Torab-Mostaedi, A. Ghaemi, H. Ghassabzadeh and M. Ghannadi-Maragheh, *Can. J. Chem. Eng.*, 2011, **89**, 1247–1254.

17 A. Ghaemi, M. Torab-Mostaedi and M. Ghannadi-Maragheh, *J. Hazard. Mater.*, 2011, **190**, 916–921.

18 A. A. M. Abdel-Karim, A. A. Zaki, W. Elwan, M. R. El-Naggar and M. M. Gouda, *Appl. Clay Sci.*, 2016, **132–133**, 391–401.

19 Y. C. Lee, A. Rengaraj, T. Ryu, H. U. Lee, H. R. An, K. S. Lee, G. W. Lee, J. Y. Kim, N. S. Heo, B. G. Kim and Y. S. Huh, *RSC Adv.*, 2016, **6**, 1324–1332.

20 Z. Cheng, Z. Gao, W. Ma, Q. Sun, B. Wang and X. Wang, *Chem. Eng. J.*, 2012, **209**, 451–457.

21 A. Krasnopyorova, D. Sofronov, A. Odnovolova, N. Efimova, G. Yuhno and O. Kogol, *Adsorpt. Sci. Technol.*, 2017, **35**, 641–646.

22 S. J. Ahmadi, N. Akbari, Z. Shiri-Yekta, M. H. Mashhadizadeh and M. Hosseinpour, *Korean J. Chem. Eng.*, 2015, **32**, 478–485.

23 S. Kasap, H. Tel and S. Piskin, *J. Radioanal. Nucl. Chem.*, 2011, **289**, 537–544.

24 S. Kasap, H. Tel and S. Piskin, *J. Radioanal. Nucl. Chem.*, 2011, **289**, 489–495.

25 S. Kasap, S. Piskin and H. Tel, *Radiochim. Acta*, 2012, **100**, 925–929.

26 S. Handley-Sidhu, T. K. Mullan, Q. Grail, M. Albadarneh, T. Ohnuki and L. E. MacAskie, *Sci. Rep.*, 2016, **6**, 4–11.

27 S. Baik, H. Zhang, Y. K. Kim, D. Harbottle and J. W. Lee, *RSC Adv.*, 2017, **7**, 54546–54553.

28 M. Caccin, F. Giacobbo, M. Da Ros, L. Besozzi and M. Mariani, *J. Radioanal. Nucl. Chem.*, 2013, **297**, 9–18.

29 J. Wang and Z. Wan, *Prog. Nucl. Energy*, 2015, **78**, 47–55.

30 Y. C. Yong, X. C. Dong, M. B. Chan-Park, H. Song and P. Chen, *ACS Nano*, 2012, **6**, 2394–2400.

31 Y. Liu, F. Liu, L. Ni, M. Meng, X. Meng, G. Zhong and J. Qiu, *RSC Adv.*, 2016, **6**, 54679–54692.

32 A. Tayyebi, M. Outokesh, S. Moradi and A. Doram, *Appl. Surf. Sci.*, 2015, **353**, 350–362.

33 S.-C. Jang, Y. Haldorai, G.-W. Lee, S.-K. Hwang, Y.-K. Han, C. Roh and Y. S. Huh, *Sci. Rep.*, 2015, **5**, 17510.

34 A. Y. Romanchuk, A. S. Slesarev, S. N. Kalmykov, D. V. Kosynkin and J. M. Tour, *Phys. Chem. Chem. Phys.*, 2013, **15**, 2321.

35 S. J. Ahmadi, N. Akbari, Z. Shiri-Yekta, M. H. Mashhadizadeh and A. Pourmatin, *J. Radioanal. Nucl. Chem.*, 2014, **299**, 1701–1707.

36 M. Hua, S. Zhang, B. Pan, W. Zhang, L. Lv and Q. Zhang, *J. Hazard. Mater.*, 2012, **211–212**, 317–331.

37 X. Huang, Z. Yin, S. Wu, X. Qi, Q. He, Q. Zhang, Q. Yan, F. Boey and H. Zhang, *Small*, 2011, **7**, 1876–1902.

38 S. Nardecchia, D. Carriazo, M. L. Ferrer, M. C. Gutiérrez and F. del Monte, *Chem. Soc. Rev.*, 2013, **42**, 794–830.

39 W. Li, S. Gao, L. Wu, S. Qiu, Y. Guo, X. Geng, M. Chen, S. Liao, C. Zhu, Y. Gong, M. Long, J. Xu, X. Wei, M. Sun and L. Liu, *Sci. Rep.*, 2013, **3**, 2125.

40 C. Li and G. Shi, *Nanoscale*, 2012, **4**, 5549.

41 Z. Chen, W. Ren, L. Gao, B. Liu, S. Pei and H.-M. Cheng, *Nat. Mater.*, 2011, **10**, 424–428.

42 X. Huang, X. Qi, F. Boey and H. Zhang, *Chem. Soc. Rev.*, 2012, **41**, 666–686.

43 Y. Xu and G. Shi, *J. Mater. Chem.*, 2011, **21**, 3311–3323.

44 D. Li, M. B. Müller, S. Gilje, R. B. Kaner and G. G. Wallace, *Nat. Nanotechnol.*, 2008, **3**, 101–105.

45 W. Gao, *Graphene Oxide: Reduction Recipes, Spectroscopy, and Applications*, 2015, vol. 39, pp. 228–240.

46 X. Dong, X. Wang, L. Wang, H. Song, H. Zhang, W. Huang and P. Chen, *ACS Appl. Mater. Interfaces*, 2012, **4**, 3129–3133.

47 F. Yavari, Z. Chen, A. V. Thomas, W. Ren, H.-M. Cheng and N. Koratkar, *Sci. Rep.*, 2011, **1**, 1–5.

48 Q. Fang, Y. Shen and B. Chen, *Chem. Eng. J.*, 2015, **264**, 753–771.

49 L. Jiang and Z. Fan, *Nanoscale*, 2014, **6**, 1922–1945.

50 M. A. Bezerra, R. E. Santelli, E. P. Oliveira, L. S. Villar and L. A. Escaleira, *Talanta*, 2008, **76**, 965–977.

51 R. L. Mason, R. F. Gunst and J. L. Hess, *Statistical Design and Analysis of Experiments*, 2015.

52 D. J. Lizotte, R. Greiner and D. Schuurmans, *J. Global Optim.*, 2012, **53**, 699–736.

53 E. Worch, *Adsorption technology in water treatment: fundamentals, processes, and modeling*, 2012.

54 A. C. Ferrari, J. C. Meyer, V. Scardaci, C. Casiraghi, M. Lazzeri, F. Mauri, S. Piscanec, D. Jiang, K. S. Novoselov, S. Roth and a. K. Geim, *Phys. Rev. Lett.*, 2006, **97**, 1–4.

55 T. Gao, H. Fjellvåg and P. Norby, *Anal. Chim. Acta*, 2009, **648**, 235–239.

56 F. T. Johra, J. W. Lee and W. G. Jung, *J. Ind. Eng. Chem.*, 2014, **20**, 2883–2887.

57 W. J. Thomas and B. Crittenden, *Adsorption Technology and Design*, 1998.

58 R. L. Mason, R. F. Gunst and J. L. Hess, *Statistical Design and Analysis of Experiments*, 2003.

59 M. I. Zaman, S. Mustafa, S. Khan and B. Xing, *J. Colloid Interface Sci.*, 2009, **330**, 9–19.